Journal of Advanced Ceramics
2024, **13**(1): 34–43
https://doi.org/10.26599/JAC.2024.9220833

Research Article

Simultaneously enhanced energy storage performance and luminance resistance in $(K_{0.5}Na_{0.5})NbO_3$-based ceramics via synergistic optimization strategy

Yu Huan[1], Diyu Gui[2], Changxiao Li[1], Tao Wei[1,✉], Lingzhi Wu[1], Xinjian Wang[3], Xiaozhi Wang[3], Zhenxiang Cheng[4,✉]

[1] *School of Materials Science and Engineering, University of Jinan, Jinan 250022, China*
[2] *Yangtze Delta Region Transformation Center for Advanced Technological Achievements, Suzhou 215000, China*
[3] *Electronic Materials Research Laboratory, Key Laboratory of the Ministry of Education and International Center for Dielectric Research, Xi'an Jiaotong University, Xi'an 710032, China*
[4] *Institute for Superconducting and Electronic Materials, Australian Institute for Innovative Materials, University of Wollongong, Innovation Campus, North Wollongong 2500, Australia*

Received: September 12, 2023; Revised: November 6, 2023; Accepted: November 26, 2023

Abstract: The rapidly advancing energy storage performance of dielectric ceramics capacitors has garnered significant interest for applications in fast charge/discharge and high-power electronic techniques. Exploring the exceptional electrical properties in harsh environments can further promote their practical applications. Defect carriers can be excited under luminance irradiation, thereby leading to degradation of energy storage performance. Herein, a synergic optimization strategy is proposed to enhance energy storage properties and luminance resistance of $(K_{0.5}Na_{0.5})NbO_3$-base (KNN) ceramics. First, the introduction of $Bi(Zn_{0.5}Ti_{0.5})O_3$ solid solution and La^{3+} ions disrupts the long-range polar orders and enhances super paraelectric relaxation characteristics. Additionally, doping La^{3+} ions can increase the band gap and reduce oxygen vacancy concentration, resulting in excellent luminance resistance. Finally, the viscous polymer process is employed to suppress the grain growth and promote chemical homogeneity. As a result, ultrahigh recoverable energy storage density (W_{rec}) of 8.11 J/cm^3 and high efficiency (η) of 80.98% are achieved under an electric field of 568 kV/cm. Moreover, the variations in W_{rec} and η are only 12.45% and 1.75%, respectively, under 500 W xenon lamp irradiation compared to the performance under a dark environment. These findings hold great potential in facilitating the practical application of dielectric ceramic capacitors in luminance irradiation environments.

Keywords: potassium–sodium niobate; energy storage performance; illumination resistance; oxygen vacancy; viscous polymer processing

1 Introduction

As an important class of functional materials, dielectric ceramics have attracted special interest in the realms of energy storage, harvesting, and conversion [1–3]. Electric energy in dielectric capacitors is stored and released through electrostatic polarization and depolarization under loading and unloading electric fields. Therefore, dielectric capacitors display promising applications in the pulsed power and high-power domains, owing to their ultrafast charge/discharge capabilities, high working voltage, and excellent high-temperature reliability [4,5]. However, the energy density of dielectric capacitors remains significantly lower than that of chemical batteries, posing a significant constraint on their broader usage in electronic devices that demand miniaturization, integration, and cost reduction. Consequently, recent efforts have been extensively directed towards enhancing the recoverable energy density of dielectric capacitors [6].

The energy storage properties of the dielectric ceramics manifest through polarization–electric (P–E) field loop. W_{rec} and η of dielectrics are determined by the following equations [5,7]: $W_{total} = \int_0^{P_{max}} E\mathrm{d}P$, $W_{rec} = \int_{P_r}^{P_{max}} E\mathrm{d}P$, $W_{loss} = W_{total} - W_{rec}$, and $\eta = (W_{rec}/W_{total}) \times 100\%$, where W_{total} and W_{loss} represent the total energy density (i.e., charged energy density) and the dissipated energy density, respectively. P, P_{max}, P_r, and E denote the real-time polarization, the maximum polarization, the remnant polarization, and the applied electrical field, respectively, obtained by the P–E loop. Consequently, achieving high W_{rec} and η in dielectric ceramics involves realizing large P_m–P_r (ΔP) and high breakdown strength (E_b) [8]. A typical improvement strategy involves disrupting the long-range-ordered domain structures of ferroelectric ceramics through solid solution doping, resulting in relaxor ferroelectric ceramics [7,9]. Relaxor ferroelectrics are characterized by a diffuse phase transition spanning a broad temperature range with four typical regions as illustrated in Fig. S1 the Electronic Supplementary Material (ESM) [8,10]. The region 1 and region 2 feature micrometer-size domains and nanoscale domains, respectively, exhibiting relatively low W_{rec} due to their small ΔP and E_b. In the region 4, when the temperature surpasses Burns temperature (T_B), the ferroelectric behavior disappears, leading to ultralow ΔP and W_{rec}. The region 3, on the other hand,

✉ Corresponding authors.
E-mail: T. Wei, mse_weit@ujn.edu.cn;
Z. Cheng, cheng@uow.edu.au

pertains to the temperature between T_m (the temperature of the maximum dielectric constant) and T_B, where dielectrics exhibit super paraelectric characteristics with polar nanoregions (PNRs). This results in high ΔP and E_b because PNRs can swiftly respond to external electric fields [11,12]. Therefore, an effective approach to enhance the energy storage properties of dielectric ceramics is to shift the region 3 towards room temperature and broaden the temperature range between T_B and T_m as much as possible. Many researches have proved that regulating the relaxor behavior in dielectric ceramics can enhance their energy storage properties [13–16]. For instance, in 15 mol% $Bi(Ni_{0.5}Zr_{0.5})O_3$ doped $(K_{0.5}Na_{0.5})NbO_3$ (KNN) ceramics, PNRs are induced, resulting in excellent energy storage properties with W_{rec} of 8.09 J/cm^3 and η of 88.46% [17].

The high energy storage density of KNN-based dielectric ceramic capacitors accelerates their applications in electrostatic energy storage [1,6,17–19]. However, several issues need to be addressed before moving towards industrial productions [5]. For instance, Especially, the luminance irradiation on the dielectric ceramic capacitors is inevitable during practical applications [20]. As is commonly understood, when the dielectric ceramics are illuminated with light possessing photo energy higher than the band gap energy (E_g), electrons in the valence band can be excited to the conduction band. This process generates free electron and hole carriers within the ceramics, which in turn can degrade the breakdown strength [13]. Therefore, enhancing E_g stands as an effective approach to optimize resistance to illumination. Additionally, an opportunity arises to simultaneously enhance E_b. As an example, incorporating the $NaNbO_3$ component with substantial E_g of 3.58 eV into $BiFeO_3$–$BaTiO_3$ ceramics leads to a significant improvement in E_b, reaching 420 kV/cm, along with W_{rec} of 8.12 J/cm^3 [21].

Herein, a synergic optimization design is explored to improve energy storage performances and luminance resistance of $0.85(K_{0.5}Na_{0.5})NbO_3$–$0.15Bi(Zn_{0.5}Ti_{0.5})O_3$–$x$%La (abbreviated as 85KNN–15BZT–xLa) ceramics, as depicted in Fig. 1. The luminance resistance is used to evaluate electrical stability of the samples under irradiation. The tolerance factor of $0.85(K_{0.5}Na_{0.5})NbO_3$–$0.15Bi(Zn_{0.5}Ti_{0.5})O_3$ is 0.93, which is permissible for a perovskite structure. In addition, the hybridization of Bi 6p and O 2p electron orbitals could enhance the polarization because of the special electron configuration of Bi^{3+} [22,23]. The selection of 85KNN–15BZT ceramics is based on their relaxor state at room temperature (Fig. S2 in the ESM) and their excellent energy storage density (Fig. S3 in the ESM). On one hand, the introduction of La^{3+} ions into the perovskite structure enhances W_{rec} and illumination resistance through the applications of relaxor strategy, defect engineering, and energy band adjustment. On the other hand, the utilization of the viscous polymer processing method (VPP) and a two-step sintering process (TSS) are implemented to improve E_b by inhibiting grain growth and optimizing chemical homogeneity. As a result, excellent energy storage performance (notably high E_b of 568 kV/cm, ultrahigh W_{rec} of 8.11 J/cm^3, and high η of 80.98%) is achieved alongside effective illumination resistance (with W_{rec} and η variations of 12.45% and 1.75%, respectively, when compared to a dark environment, under the irradiation of 500 W xenon lamp) in the 85KNN–15BZT–1La ceramics fabricated using VPP. This work presents promising prospects for applications in advanced pulsed power techniques.

2 Experimental

85KNN–15BZT–xLa (x = 0, 0.5, 1, 1.5, 2) powders were synthesized by the traditional solid-state reaction method. Analytically pure powders of Na_2CO_3 (99.8%), K_2CO_3 (99.8%), Bi_2O_3 (99.8%), La_2O_3 (99.8%), TiO_2 (99.8%), ZnO (99.5%), and Nb_2O_5 (99.9%) produced by Shanghai Macklin Biochemical Co., Ltd. were homogenized for 12 h in a planetary milling using ethyl

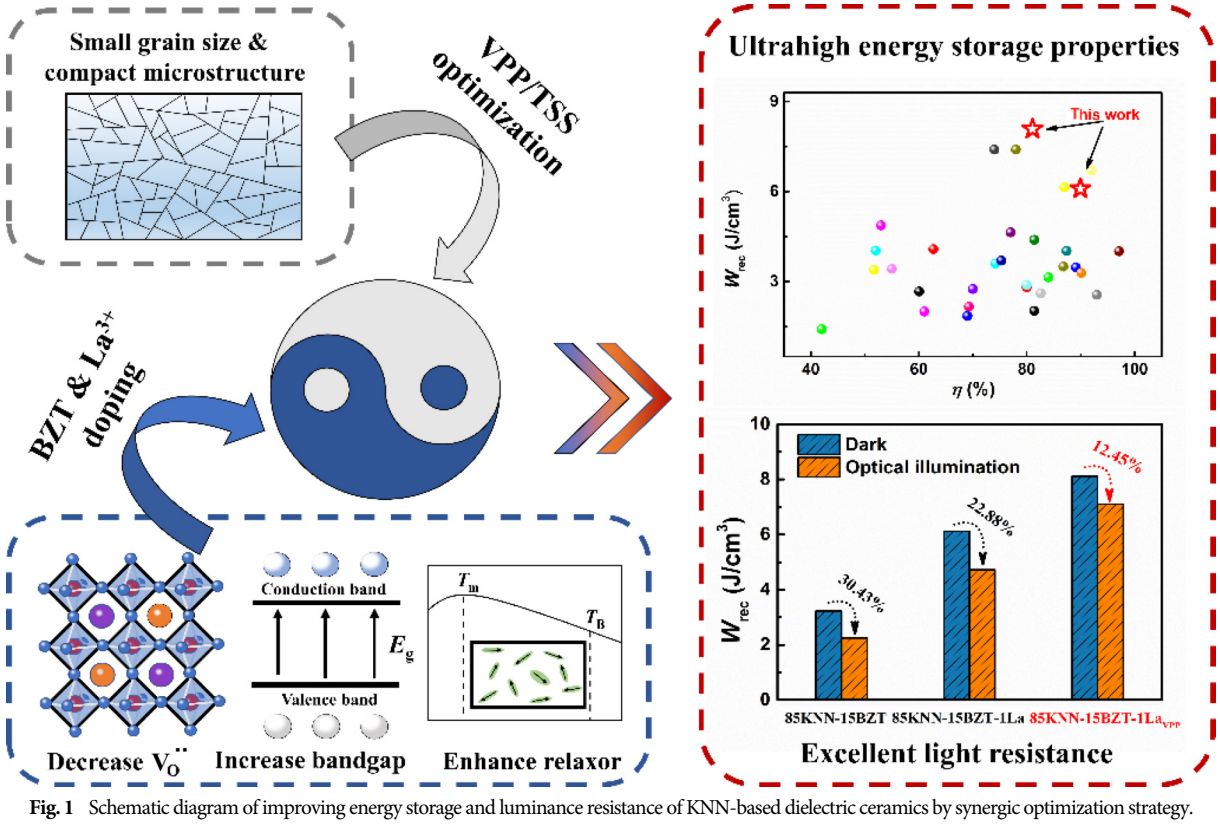

Fig. 1 Schematic diagram of improving energy storage and luminance resistance of KNN-based dielectric ceramics by synergic optimization strategy.

清華大学出版社 Tsinghua University Press | SciOpen

alcohol as medium. The powder mixtures were calcined twice at 850 ℃ for 3 h with intermediate milling. Subsequently, the powders were ball milled for 12 h. The powders were mixed with a polyvinyl butyral binder and then were compacted into pellets (diameter of ~8 mm and thickness of ~0.8 mm). The green pellets were sintered by a two-step sintering strategy at a heating rate of 3 ℃/min in a sealed crucible full of the calcined powders to minimize the evaporation of alkaline metals. The crucible is filled with the calcined powders of the same composition. Before the electric measurement, the samples were polished and thinned to ~70 μm. Then, Au electrodes with an area of 15.9 mm^2 were deposited onto the two main surfaces of the sintered disk samples by radio frequency magnetron sputtering. To assess the luminance resistance of the samples, a thin-film electrode composed of indium tin oxide (ITO) was sputtered onto one side of the ceramic sample.

VPP was tried in the 85KNN–15BZT–1La component. First, the slurry for the VPP process was prepared by mixing the calcined powders (70 wt%), solvent (mixture of 12 wt% anhydrous alcohol and 4 wt% glycerin), binder (polyvinyl alcohol: 14 wt%) in a planetary mill for 12 h. Secondly, the thickness of the mixture was gradually thinned to 0.4 mm via repeated rough roll forming and aging. Finally, the green ceramic tape was precisely rolled forming 0.06 mm and punched into discs with a diameter of 8 mm. The ceramic green pellets were then densified using the two-step sintering strategy with a heating rate of 3 ℃/min. The zirconia plate was pressed against the green ceramics during the sintering stage. Green compacts were heated to 600 ℃ and held for 10 h to remove the organic binder. All the green ceramics were sintered using the TSS process, outlined in Fig. S4 in the ESM. The sintering temperature and holding times are listed in Table S1 in the ESM. The thickness of the samples is 50 μm.

The characterizations were described in detail in the ESM.

3 Results and discussion

The temperature-dependent dielectric constant (ε) and dielectric loss (tanδ) curves were conducted for 85KNN–15BZT–*x*La ceramics at different frequencies, as shown in Fig. 2(a), to reveal phase transitions and relaxor behaviors. The diffuse phase transition, with a wide dielectric peak and a frequency-dependent dielectric response, indicates strong dielectric relaxation in 85KNN–15BZT–*x*La ceramics [16,24]. With an increase in the La^{3+} content, the ε–temperature curves become flatter, and T_m shifts towards low temperatures, suggesting improved relaxor behavior. In the case of the 85KNN–15BZT–1La ceramics, T_m obtained from the temperature-dependent ε curve at 1 MHz in Fig. 2(a) and T_B obtained from in Fig. 2(b) locate at about –30 and 224 ℃, respectively. It demonstrates that the ceramics over a broad temperature range locate in the region 3 (Fig. S1 in the ESM) and exhibit a super paraelectric characterization. Besides, the suppressed dielectric peak indicates the enhanced thermal stability of ε, which is also desirable for the high-temperature capacitors. The modified Curie–Weiss law is generally employed to quantitatively estimate the dielectric relaxation properties according to the equation: $1/\varepsilon_r - 1/\varepsilon_{max} = (T - T_m)^\gamma / C$, where

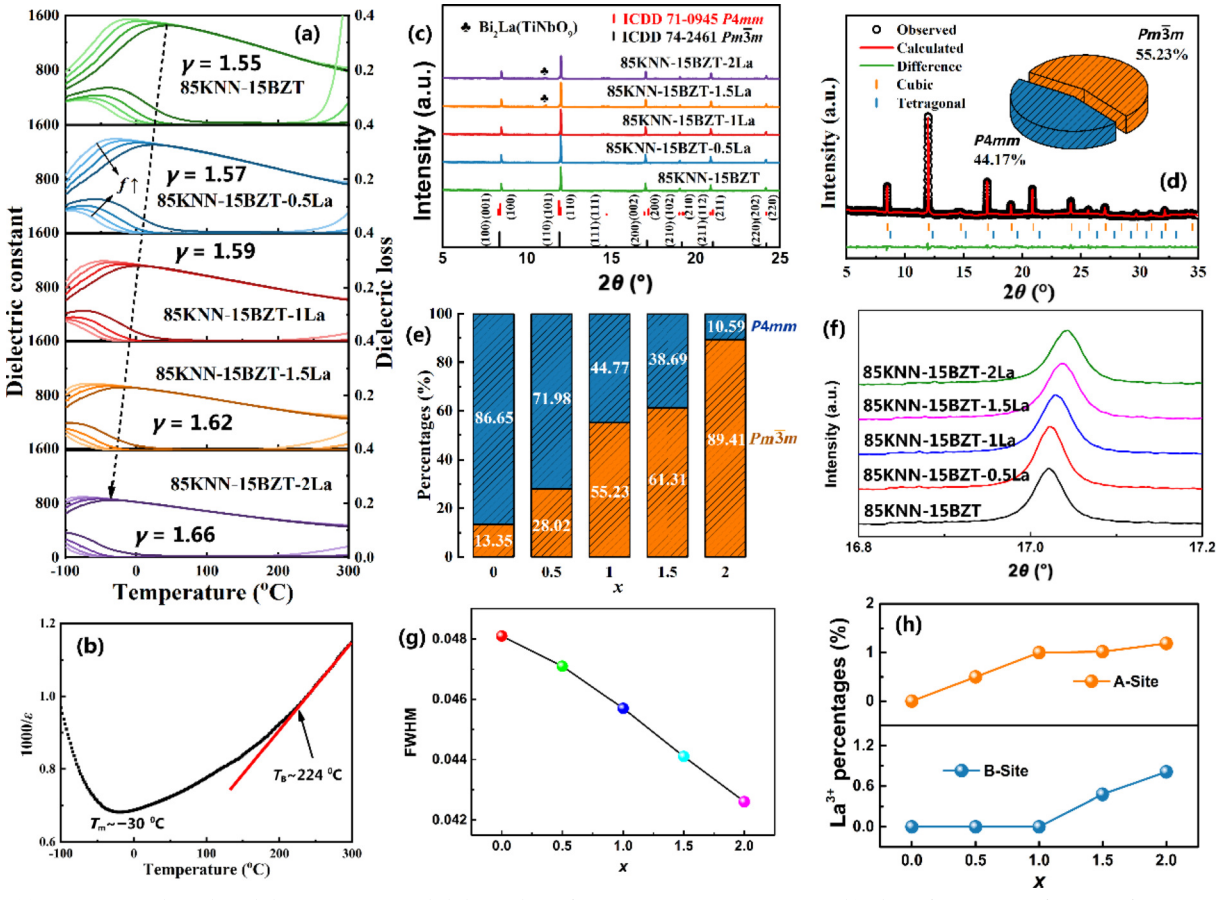

Fig. 2 (a) Temperature dependent dielectric constant and dielectric loss of 85KNN–15BZT–*x*La ceramics. (b) Plots of 1000/ε as a function of temperature for 85KNN–15BZT–1La ceramics at 1 MHz and corresponding T_B value. (c) High-resolution synchrotron XRD patterns in 2θ range of 5°–25° (λ = 0.059076 nm). (d) Synchrotron XRD Rietveld refinement results for sample of x = 1. (e) Phase fractions of 85KNN–15BZT–*x*La ceramic samples. (f) Enlarged synchrotron XRD patterns in 2θ range of 16.8°–17.2°. (g) FWHM of (200) diffraction peaks as a function of x. (h) Occupied percentage of La^{3+} ion in A and B sites as a function of x.

T_m, γ, and C are the temperature corresponding to ε_{max}, the diffusion factor, and the Curie-like constant, respectively [25,26]. The fitting results for all samples are plotted in Fig. S5 in the ESM, and the γ values are listed in Fig. 2(a). It is well-known that the normal ferroelectrics and ideal relaxor ferroelectrics show the γ value of 1 and 2, respectively [27,28]. Therefore, the monotonic increment in γ from 1.55 at x = 0 to 1.66 at x = 2 reveals the doping La^{3+} ions improve the relaxor behavior of the 85KNN–15BZT–xLa ceramics. It is observed the relatively low tanδ (< 0.1) over the temperature range and over a wide frequency range from 40 Hz to 1 MHz (Fig. S6 in the ESM) implying excellent insulation capability and the potential for high dielectric breakdown strength [29]. Notably, an excellent frequency stability of ε with a small variation of 3% is achieved for all the samples, as shown in Fig. S6 in the ESM. The ε value decreases rapidly as the doping of La^{3+} ions increases, and the Curie peak shifts towards low temperatures, as indicated by the arrow in Fig. 2(a). Both observations suggest that the La^{3+} ions enter the perovskite lattice and influence the phase transition.

Subsequently, the crystal structure of the samples is accurately determined using high-resolution synchrotron X-ray diffraction (XRD) measurements, as presented in Fig. 2(c). Vertical lines indicate the standard diffraction peaks of $(K,Na)NbO_3$ with $Pm\bar{3}m$ and $P4mm$ symmetries for comparison. All samples exhibit the main perovskite crystalline structure. A secondary phase of $Bi_2La(TiNbO_9)$ is observed in 85KNN–15BZT–1.5La and 85KNN–15BZT–2La ceramics. This observation indicates that La has limited solubility in the 85KNN–15BZT ceramics, tending to dissolve at a concentration of up to ~1% mol. To further comprehend the variation in local structure for 85KNN–15BZT–xLa ceramics with different La content, the synchrotron XRD patterns are fitted using fixed background, synchrotron instrument information, and peak type. This approach allows the extraction of lattice parameters, phase fraction, refinement parameters, atomic occupation, and La^{3+} ionic coordinates, as summarized in Tables S2–S4 in the ESM. The experimental lines are well-fitted with calculated lines, as shown in Fig. 3(d) and Fig. S7 in the ESM. In addition, the weighted profile (R_{wp}) and profile reliability (R_p) factors are both smaller than 10%, confirming the reliability of the XRD refinement. The coexistence of cubic and tetragonal phase structures is confirmed through the XRD Rietveld refinement, and the phase fractions are listed in Fig. 2(e). The c/a ratio decreases as the La content increases, as summarized in Table S3 in the ESM, implying the reduction of the crystal distortion. Additionally, the (200) peaks at approximately 17° are shown in Fig. 2(f). The full-width at half maxima (FWHM) of the (200) diffraction peak monotonously decreases as the La content increases in Fig. 2(g), which reflects the low asymmetric structure of the crystal and the small lattice distortion. The high proportion of the cubic structure and the small crystal distortion in the 85KNN–15BZT–1La ceramics suggest the ceramic features a super paraelectric state.

The occupation of La^{3+} ions within the perovskite lattice is determined through the XRD Rietveld refinement, as depicted in Fig. 2(h). This allows us to infer the defect configuration in the ceramics. When the KNN-based ceramics are sintered at high-temperature, Bi^{3+} tends to volatilize along with the loss of their associated oxides (Bi_2O_3), leading to the formation of A-site vacancy ($V_{Bi}^{'''}$) and oxygen vacancy ($V_O^{\cdot\cdot}$), which can be expressed using Eq. (1):

$$2Bi_{Bi}^{\times} + 3O_O^{\times} \rightarrow V_{Bi}^{'''} + 3V_O^{\cdot\cdot} + Bi_2O_3 \quad (1)$$

The defect configuration of the 85KNN–15BZT sample is illustrated in Fig. 3(a1). For $x \le 1$, La^{3+} ions show a preference for occupying the A-sites due to their similar ion radius and chemical valence state, which is similar to what was reported previously [30]. Furthermore, this preference is supported by the expanded lattice parameters (Table S2 in the ESM), where the ionic radius (R) of La^{3+} ion (1.50 Å) with coordination numbers (CNs) of 12 is larger than the equivalent ionic radius of A-site ions (1.42 Å, calculated by 0.425 × R (K^+, 1.64 Å) + 0.425 × R (Na^+, 1.39 Å) + 0.15 × R (Bi^{3+}, 0.9 Å). As a result, La^{3+} ions tend to occupy $V_{Bi}^{'''}$. Simultaneously, the introduction of O^{2-} ions from La_2O_3 supplements the oxygen deficiency. The defect reaction equation can be expressed as Eq. (2):

$$La_2O_3 + 2V_{Bi}^{'''} + 3V_O^{\cdot\cdot} \rightarrow 2La_{Bi}^{\times} + 3O_O^{\times} \quad (2)$$

It results in the point defect of $2La_{Bi}^{\times}$ in the 85KNN–15BZT–0.5La and 85KNN–15BZT–1La ceramics as sketched in Fig. 3(a2). When the La^{3+} content exceeds 1 mol%, the increase in the percentage of La^{3+} ions at the A-site starts to deviate from linear behavior, as seen in Fig. 2(h). This deviation is due to the limitations of solid solution, indicating the initiation of the replacement of the B-site by La^{3+} ions. The perspective aligns with the further expansion of lattice parameters (Table S2 in the ESM) attributed to the larger ion radius of La^{3+} ion (1.172 Å) with 6 CNs compared to Nb^{5+} (0.78 Å), Ni^{2+} (0.83 Å), and Zr^{4+} (0.86 Å), each with 6 CNs. The incorporation reaction of La ions into the B-site can be expressed using Eq. (3):

$$La_2O_3 \rightarrow 2La_{Nb}^{''} + 2V_O^{\cdot\cdot} + 3O_O^{\times} \quad (3)$$

Consequently, the defect structures, including oxygen vacancies ($V_O^{\cdot\cdot}$) and cation substitution ($La_{Nb}^{''}$ and $2La_{Bi}^{\times}$), are present in 85KNN–15BZT–1.5La and 85KNN–15BZT–2La ceramics, as depicted in Fig. 3(a3). In summary, the concentration of oxygen vacancies first decreases and then increases, reaching the minimum value when x = 1.

To further semi-quantify the concentration of $V_O^{\cdot\cdot}$ in the 85KNN–15BZT–xLa ceramics, high-resolution X-ray photoelectron spectroscopy (XPS) spectra of O 1s were performed, as shown in Fig. 3(b). Each O 1s spectrum is fitted using Lorentz function with two peaks. The black, red, and green lines represent the observational (Obs), fitting (Fit), and base (Bac) lines, respectively. The binding energy at ~529.31 eV corresponds to lattice oxygen ions, while the peak centered at ~530.95 eV is associated with oxygen vacancy [31–33]. The ratios of their peak areas are presented in Fig. 3(b). The $V_O^{\cdot\cdot}$ ratio decreases from 27.26% to 24.43%, and subsequently increases to 25.65% as the La concentration increases from 0 to 2 mol%. Notably, the ceramics with the 85KNN–15BZT–1La composition exhibit the lowest oxygen vacancy concentration, aligning with the results from XRD Rietveld refinement.

Impedance spectra of 85KNN–15BZT–xLa samples, measured within the frequency range from 100 mHz to 1 MHz at a constant temperature of 600 ℃, are exhibited in Fig. 3(c). In this figure, Z' and Z'' represent the real and imaginary components of the complex impedance (Z^*), respectively. Each composition exhibits only one semicircle and approaches the zero intercept horizontally at high frequencies. This similarity suggests that the grain and grain boundary display comparable conductivity behavior, making them challenging to distinguish [34]. Among the samples, the Z^* semicircle of the 85KNN–15BZT–1La sample exhibits the largest radius, indicating the highest resistance among the

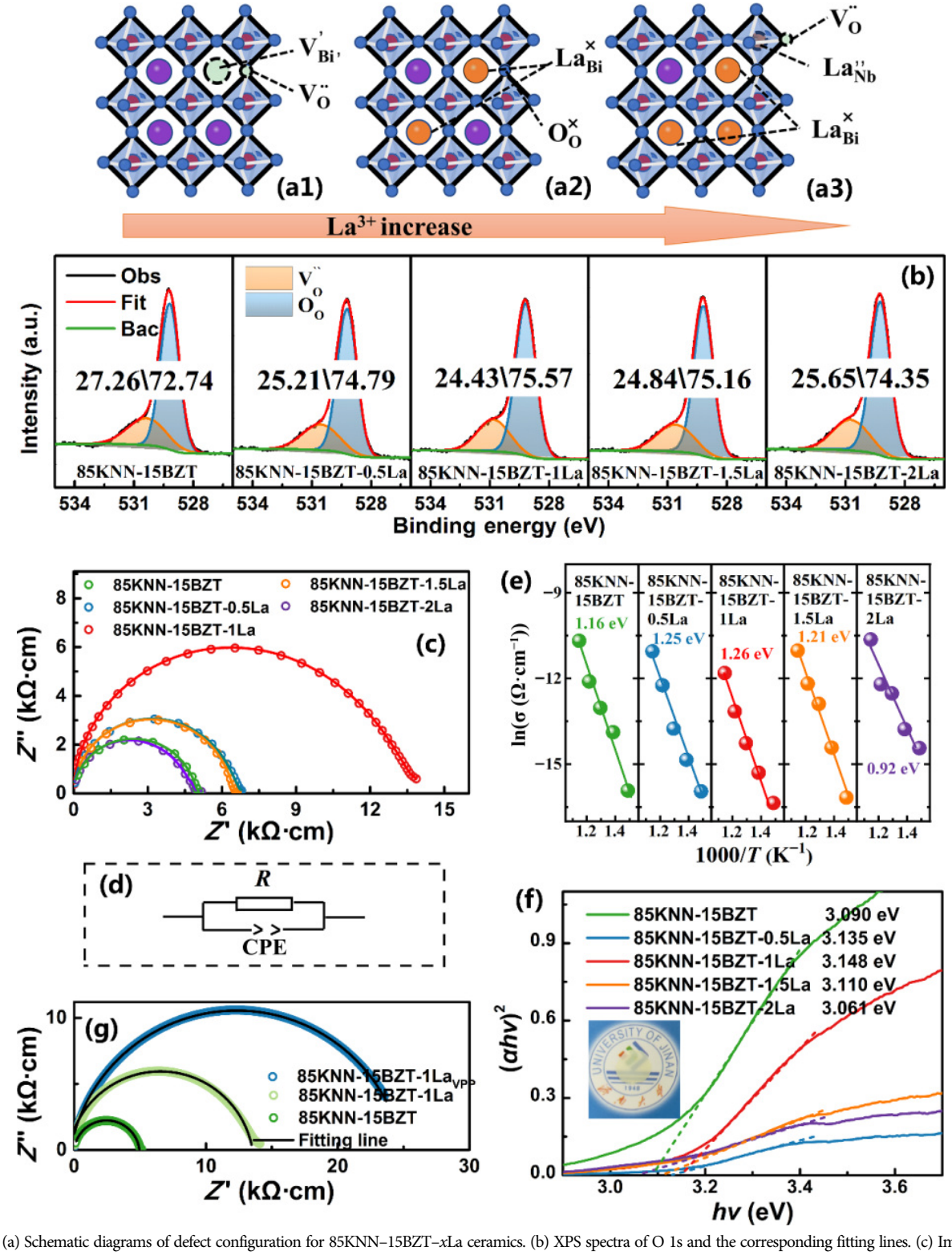

Fig. 3 (a) Schematic diagrams of defect configuration for 85KNN–15BZT–*x*La ceramics. (b) XPS spectra of O 1s and the corresponding fitting lines. (c) Impedance spectra of 85KNN–15BZT–*x*La ceramics at 600 ℃. (d) Equivalent circuit proposed for 85KNN–15BZT–*x*La ceramics. (e) Arrhenius plots of conductivity vs. 1000/*T* and the corresponding activation energy. (f) Plots of $(\alpha h\nu)^2$ vs. $h\nu$ of 85KNN–15BZT–*x*La ceramics; the inset is intuitive picture through 85KNN–15BZT–1La sample. (g) Impedance spectra of 85KNN–15BZT, 85KNN–15BZT–1La, and 85KNN–15BZT–1La$_{VPP}$ samples under 600 ℃ and corresponding fitting lines.

85KNN–15BZT–1La ceramics. Nyquist plots of 85KNN–15BZT–*x*La samples at different temperatures (400–600 ℃), as shown in Fig. S8 in the ESM, are carried out to elucidate their electrical conduction behavior. An assumed equivalent circuit (depicted in Fig. 3(d)) consisting of the resistance (*R*) and constant phase element (CPE) (which replaces the standard capacitance *C* element due to the complex plane plots being slightly depressed instead of centred on the abscissa axis, namely Debye's model [35]) is proposed. This model provides a better fit to the experimental data [36]) and is proposed to fit the impedance spectra [37]. The excellent agreement between the experimental and fitting curves validates the reliability

of the electrical equivalent circuit and confirms the electrical homogeneity of both grain and grain boundary. The calculated conductivity (σ) obtained from simulated R_g is plotted in Fig. 3(e). lnσ shows a linear relationship with 1000/T, demonstrating that the conductivity is commonly governed by Arrhenius law. This law can be expressed by the equation: $\sigma = \sigma_0 \exp(-E_a/k_B T)$, where E_a is the activation energy, σ_0 is the high-temperature limit of the conductivity, k_B is the Boltzmann constant, and T is the temperature in Kelvin scale. Arrhenius plots of the 85KNN–15BZT–xLa samples are plotted in Fig. 3(e). In previous studies, the activation energy in the range of 0.6–1.3 eV are associated with ionized oxygen vacancies [10,38–41], aligning with the XPS results and defect chemistry analysis. The trend of E_a as a function of x exhibits a similar tendency with the resistance, which supports the lowest oxygen vacancy concentration in the 85KNN–15BZT–1La sample. This is because the activation energy is linked to the creation and migration of free energy of charge carriers over extended distances [42]. The high resistance and E_a values of the 85KNN–15BZT–1La sample are attributed to the low defect concentration, contributing to its excellent electrical properties, including low dielectric loss, large breakdown electric field, and excellent energy storage performance.Ultraviolet–visible (UV–Vis) absorption spectra of 85KNN–15BZT–xLa ceramics are presented in Fig. S9 in the ESM. A strong absorption band is detected when the wavelength is shorter than ~430 nm for all the samples. This can be attributed to electron transition from the valance band to the conduction valance. E_g is calculated using Tauc plot [43] following the equation: $(\alpha h\upsilon)^{1/2} = A(h\upsilon - E_g)$, where α is the absorption coefficient, h is the Plank constant, υ is the photon frequency, and A is the constant. The intersection of the plots with the x-axis represents E_g, as illustrated in Fig. 3(f). Notably, the E_g value steadily increases from 3.090 to 3.148 eV, and then decreases to 3.061 eV with increasing La doping. The variation in the E_g value should be correlated with oxygen vacancy concentration and the replacement of La^{3+} in ABO_3 lattice. Moreover, the reduction observed when $x > 1$ is also related to the emergence of an impurity ($Bi_2La(TiNbO_9)$) phase [44]. The E_b value was closely related to E_g. Here, the relationship between intrinsic E_b and E_g can be expressed by the following formula: $E_b = 1.36\times10^7\times(E_g/4.0)^3(\mathrm{V/cm})$ [3]. Therefore, E_b is directly proportional to E_g. Consequently, the high E_g values lead to high breakdown strength [13] and excellent resistance to illumination. In addition, the optical characteristics of the 85KNN–15BZT–1La ceramics could be clearly discerned through the samples with a thickness of ~0.10 mm as displayed in the insets of Fig. 3(f).

To intuitively observe the domain configuration in the 85KNN–15BZT–xLa ceramics, the microstructural analysis was conducted using a bright-field transmission electron microscope (TEM). Within the grains, a representative domain structure of a miniaturized lamellar shape, with a width of around 10–20 nm (indicated by the yellow lines in Fig. 4(a)), was observed. This structure accounts for the considerable ferroelectricity of the 85KNN–15BZT sample [11,24]. The introduction of a small amount of La dopant (x = 1) transforms the lamellar domain into featureless nanodomain (PNRs), as indicated by the yellow circle in Fig. 4(b). This transformation is a typical characteristic of relaxor behavior [45,46]. The introduction of La^{3+} ions disrupts the ordered arrangement of cations, increases the disorder of the crystal structure, enhances the relaxor behavior, and thus triggers the emergence of PNRs. The VPP process further disrupts the ferroelectric polar order and reduces the size (2–6 nm) of PNRs as shown in Fig. 4(c), which might be related to the suppressed grain growth. These PNRs respond rapidly to applied electric fields and readily return to their initial state upon the removal of the electric field. The TEM results are consistent with the dielectric properties vs. temperature curves.

Piezoelectric force microscopy (PFM) was employed to intuitively reveal the compositional dependence of dielectric relaxor nature through local poling experiments. A direct current (DC) voltage of 9 V is applied to the tip with a scan of a 1 μm × 1 μm area to assess polarization switching. Out-of-plane PFM amplitude images of the 85KNN–15BZT and 85KNN–15BZT–1La samples are recorded immediately after the removal of DC tip-bias and again after a relaxation period of 10 min, as shown in Figs. 4(d1) and 4(d2) and Figs. (4e1) and 4(e2), respectively. These images were examined to analyze the stability of the induced macroscopic domains. Both samples displayed oriented macroscopic domains, indicating that the applied voltage triggers reversible polarization switching, consistent with the macroscopically measured polarization hysteresis. However, the observed microscopic switching domains in this work are relatively limited compared to other ferroelectric ceramics [11,47], indicating a relatively small remnant polarization for 85KNN–15BZT–xLa ceramics. The PFM signal from induced microdomains in the 85KNN–15BZT sample remains stable, whereas the signals of switched domains in 85KNN–15BZT–1La samples quickly relax to their initial state and can hardly be detected after 10 min. This result confirms that the relaxation behavior of the 85KNN–15BZT–1La sample is stronger than that of the 85KNN–15BZT sample. The rapid reversibility of PNRs in the 85KNN–15BZT–1La sample results in nearly imperceptible remnant polarization, thereby enhancing energy storage efficiency.

To further enhance the compactness and homogeneity of the ceramics on the microscopic scale, the 85KNN–15BZT–1La sample was prepared using VPP. A comparison of the microscopy of the 85KNN–15BZT–1La and 85KNN–15BZT–$1La_{VPP}$ samples was conducted using TEM. Both samples exhibited uniform grain size and dense microstructure due to the close arrangement of the grains and distinct grain boundaries. However, the average grain size of the 85KNN–15BZT–$1La_{VPP}$ sample (~260 nm, Fig. 4(f)) is notably smaller than that of the 85KNN–15BZT–1La sample (~310 nm, Fig. 4(g)). SEM exhibits the similar grain size behavior as shown in Fig. S10 in the ESM. Smaller grain size in ceramics usually correspond to more compact microstructures [48] and smaller PNR size, typically ranging from around 2–6 nm (Fig. 4(c)) [49]. The fine grain size and dense microstructure contribute to enhanced breakdown strength and energy storage density. The presence of small PNRs enables rapid responses to applied electric fields and easily restoration to the initial state after the electric field is removed, resulting in the high energy storage efficiency.

Chemical heterogeneity was investigated using a high-angle annular dark field combined with scanning transmission electron microscopy (HAADF-STEM) and energy dispersive spectroscopy (EDS). Bi-element maps of several grains in the 85KNN–15BZT–1La and 85KNN–15BZT–$1La_{VPP}$ samples are shown in Figs. 4(h2) and 4(i2), respectively. Clear micro segregation of Bi element is observed at the grain boundary in the 85KNN–15BZT–1La sample, corresponding to lighter regions in the HAADF-STEM image. Meanwhile, other elements are evenly distributed within the grain, as shown in Fig. S11 in the ESM. This phenomenon is attributed to insufficient element diffusion during the preparation process [50]. In contrast, the HAADF-STEM results and the corresponding elemental analysis reveal a

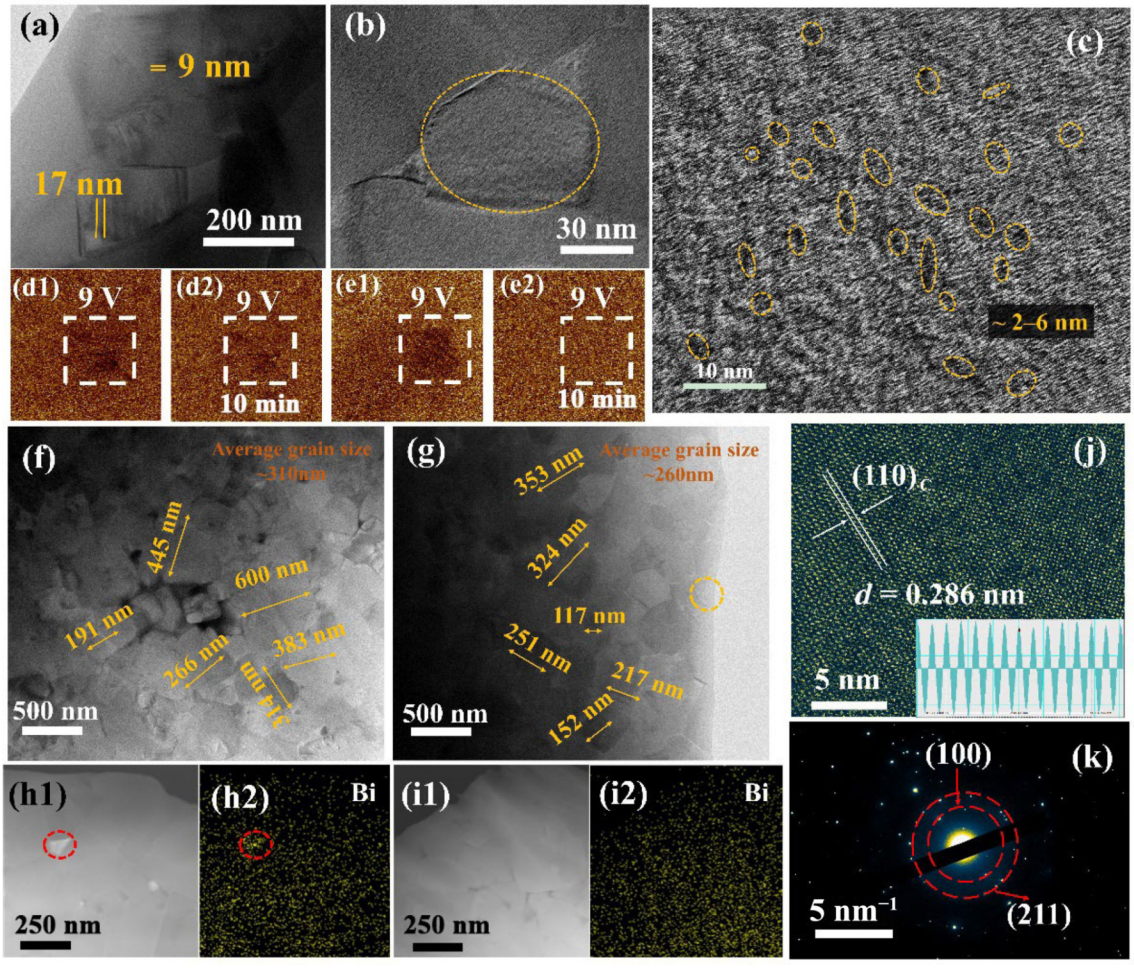

Fig. 4 Domain configuration of (a) 85KNN–15BZT, (b) 85KNN–15BZT–1La, and (c) 85KNN–15BZT–1La$_{VPP}$ ceramics. Out-of-plane PFM amplitude images of (d) 85KNN–15BZT and (e) 85KNN–15BZT–1La sample recorded directly after poling with 9 V in 1 μm × 1 μm region and after a period of 10 min. Overview TEM images of (f) 85KNN–15BZT–1La and (g) 85KNN–15BZT–1La$_{VPP}$ ceramics. HAADF–STEM image and the corresponding EDS mapping image of Bi element for (h) 85KNN–15BZT–1La and (i) 85KNN–15BZT–1La$_{VPP}$ ceramics. (j) HRTEM image and (k) SAED image of 85KNN–15BZT–1La$_{VPP}$ ceramics.

homogenous distribution of the Bi element in the 85KNN–15BZT–1La$_{VPP}$ samples. This indicates that VPP can facilitate the chemical uniformity, thereby benefiting the electrical properties. The resistance of the 85KNN–15BZT–1La$_{VPP}$ sample is significantly higher than that of the 85KNN–15BZT–1La sample, as observed in Nyquist plots in Fig. 3(g). This observation points to robust electrical properties of the 85KNN–15BZT–1La$_{VPP}$ ceramics.

Furthermore, distinct lattice fringes are evident in a high-resolution transmission electron microscopy (HRTEM) image, as shown in Fig. 4(j). The measured interplanar spacing is about 0.286 nm, corresponding to the (110) planes (refer to PDF No. 32-0822) of the KNN-based ceramics. Sharp diffraction rings from the (100) and (211) crystal planes are indexed in a selected area electron diffraction (SAED) image in Fig. 4(k). These results collectively confirm the good crystallinity of the 85KNN–15BZT–1La$_{VPP}$ ceramic, consistent with the XRD findings.

To evaluate the energy storage performance of the 85KNN–15BZT–*x*La ceramics, the electric field-dependent unipolar *P*–*E* loops are depicted in Fig. S12 in the ESM. The calculated W_{rec}, η, and E_b are summarized in Table S5 in the ESM. P_{max} of each composition increases monotonically with increasing the electrical field, attributed to the transition between PNRs and long-range ferroelectric domains. However, P_{max} at similar electric field strength decreases due to the reduction of the crystal symmetry (indicated by the decreasing *c*/*a* ratio in Table S2 in the ESM). P_r of 85KNN–15BZT–1La consistently maintains relatively low values due to the combined contributions of improved relaxor characteristics and low leakage current resulting from a reduced defect concentration. The substantial E_b plays an essential in achieving ultrahigh W_{rec}. Herein, Weibull distribution analysis is employed to evaluate E_b of ceramics using the equations: $X_i = \ln E_i$, $Y_i = \ln(\ln(1/(1-P_i)))$, $P_i = i/(n+1)$, where E_i represents the specific breakdown strength for the *i*th sample arranged in ascending order, P_i denotes the probability of dielectric breakdown, and *n* indicates the total number of the samples [16]. As depicted in Fig. 5(c), the fitting results exhibit a linear relationship between X_i and Y_i with shape parameter β exceeding 14, indicating high reliability. The average E_b extracted from fitting results increases from 284 kV/cm for $x = 0$ to 480 kV/cm for $x = 0.1$. Because of the combined effects of P_{max}, P_r, and high E_b, the 85KNN–15BZT–1La sample achieves the most favorable comprehensive energy storage properties, characterized by ultrahigh W_{rec} of 6.12 J/cm^3 and η of 89.87% at E_b of 478 kV/cm, as shown in Fig. 5(b).

In comparison to the 85KNN–15BZT–1La sample, the 85KNN–15BZT–1La$_{VPP}$ sample exhibits slimmer unipolar *P*–*E* loops (Fig. 5(a)), a result of the rapid response of PNRs to external electrical fields. What is more, it demonstrates higher E_b of

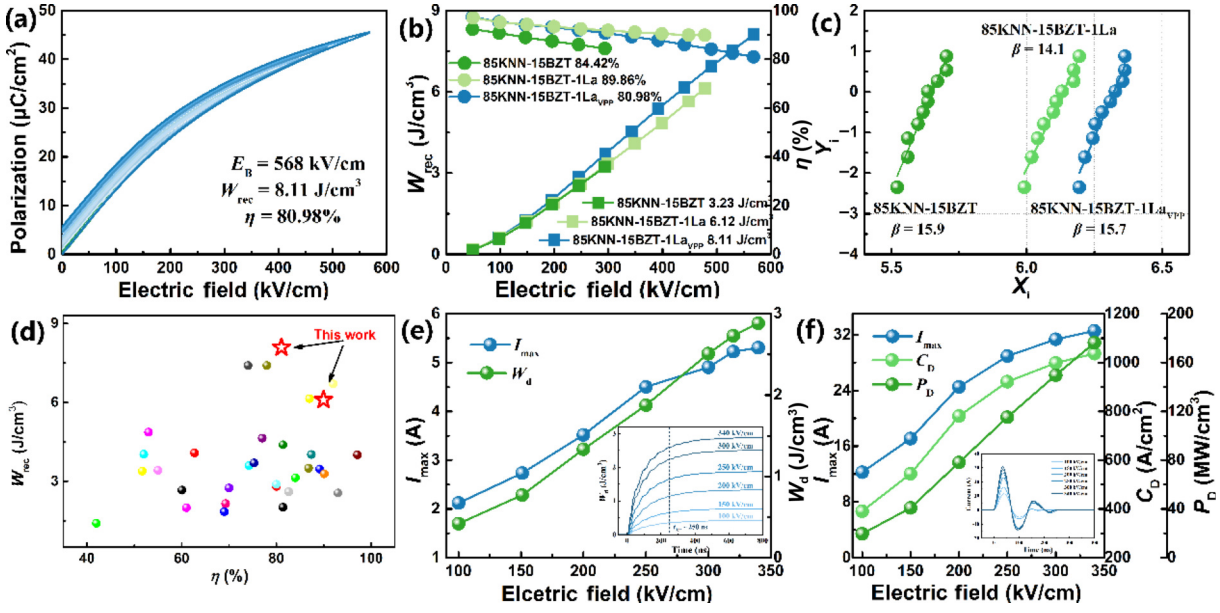

Fig. 5 (a) Unipolar *P*–*E* loops of 85KNN–15BZT–1La$_{VPP}$ ceramics. (b) W_{rec} and η as a function of applied electric field for 85KNN–15BZT, 85KNN–15BZT–1La, and 85KNN–15BZT–1La$_{VPP}$ ceramics. (c) Weibull distribution plots and fitting lines. (d) Comparison of W_{rec} among 85KNN–15BZT–1La, 85KNN–15BZT–1La$_{VPP}$, and other reported KNN-based ceramic capacitors. (e) Overdamped and (f) underdamped charge–discharge properties and corresponding curves of 85KNN–15BZT–1La$_{VPP}$ ceramics.

580 kV/cm (Fig. 5(c)), attributed to the high chemical homogeneity and compact microstructure. Both factors contribute to excellent W_{rec} of 8.11 J/cm³ and η of 80.98 % at E_b of 568 kV/cm. To evaluate the significance of these results, key parameters of the 85KNN–15BZT–1La, 85KNN–15BZT–1La$_{VPP}$ samples, and other reported KNN-based ceramic capacitors are presented in Fig. 5(d). Details, including the composition, W_{rec} and η, and relevant references for other reported KNN-based ceramic capacitors, are listed in Table S6 in the ESM. The 85KNN–15BZT–1La$_{VPP}$ sample simultaneously achieves ultrahigh W_{rec} and high η, surpassing the performance of most reported KNN-based ferroelectric ceramic capacitors. This demonstrates that the prepared KNN-based ceramics represent the state-of-the-art in ferroelectric capacitors.

Temperature reliability regarding energy storage performances is crucial for the practical applications of ceramic capacitors. Figure S13 in the ESM depicts the temperature-dependent unipolar *P*–*E* loops of 85KNN–15BZT–1La$_{VPP}$ at 400 kV/cm and 10 Hz. It is evident that the insulation properties gradually weaken with increasing temperature due to defects activated by elevated temperatures. This phenomenon is consistent with the decrease in resistivity (Fig. 3(c)) and the sharp rise in tanδ (Fig. 2(a)). The variations in W_{rec} and η remain below 20% and 10% (Fig. S14 in the ESM), respectively, across the entire temperature range from 25 to 150 ℃. This indicates that the prepared ceramic exhibits positive temperature stability in energy storage performance. Pulse charge–discharge performance is a crucial factor for practical applications. Figures 5(e) and 5(f) present the charge–discharge performance of the 85KNN–15BZT–1La$_{VPP}$ sample as a function of applied electric fields. The inserts depict the corresponding overdamped and underdamped curves at different electric fields. The quick release time of 90% energy ($t_{0.9}$) of ~250 ns indicates the excellent overdamped discharge performance of the 85KNN–15BZT–1La$_{VPP}$ sample. The fast discharge rate can be attributed to the PNRs' fast response to external electric fields. The discharge energy density (W_d) is calculated using the equation: $W_d = R\int i(t)^2 dt/V$, where R, $i(t)$, and V are the load resistor (300 Ω), real-time current, and volume, respectively. The 85KNN–15BZT–1La$_{VPP}$ sample achieves high W_d of 2.88 J/cm³ at 340 kV/cm. W_d is smaller than W_{rec} because of the viscous force of domain wall motion. In a hypothetical viscous medium, the switching speed of domain walls will be reduced by viscous forces (F_v) [51,52]. Under the measurement condition of *P*–*E* loops, the domain walls move slowly so that F_v generates a slight effect on domain wall movement. Nevertheless, in the charge–discharge process, F_v has a great influence on the domain wall, which results in the decrease of the discharged energy [53]. The power density (P_D) can be calculated according to the equation: $P_D = (EI_{max})/2S$, where E, I_{max}, and S are the electric field, the maximum current, and the electrode area, respectively. It can be observed that P_D of the 85KNN–15BZT–1La$_{VPP}$ sample reaches the maximum of 176 MW/cm³ at 340 kV/cm. High W_d and P_D highlight the promising application potential of these ceramics in pulsed capacitors.

Illumination resistance of the 85KNN–15BZT, 85KNN–15BZT–1La, and 85KNN–15BZT–1La$_{VPP}$ samples is evaluated by measuring their unipolar *P*–*E* loops both in a dark environment and under irradiation with 500 W xenon light. The distance between the xenon lamp and the sample is 20 cm. W_{rec}, η, and E_b values were calculated and compared in Fig. 6. In all samples, the unipolar *P*–*E* loops exhibit larger P_m and P_r under optical illumination compared to those in the dark environment. This behaviour can be attributed to the excitation of electrons in the valence band by the high-energy radiation, leading to their injection into the conduction band. These charge carriers then migrate under the influence of the applied electric field, contributing to larger P_m. A portion of these charge carriers becomes trapped when the electric field is removed, resulting in observed larger P_r. For instance, in the case of 85KNN–15BZT, P_m increased from 12.8 to 15.1 μC/cm² at a fixed electric field of 100 kV/cm when the sample was illuminated, while P_r sharply increased from 0.96 to 3.11 μC/cm² (Fig. 6(a)). In 85KNN–15BZT–1La, the number of excited electrons was lower compared to 85KNN–15BZT due to higher E_g for 85KNN–15BZT–1La

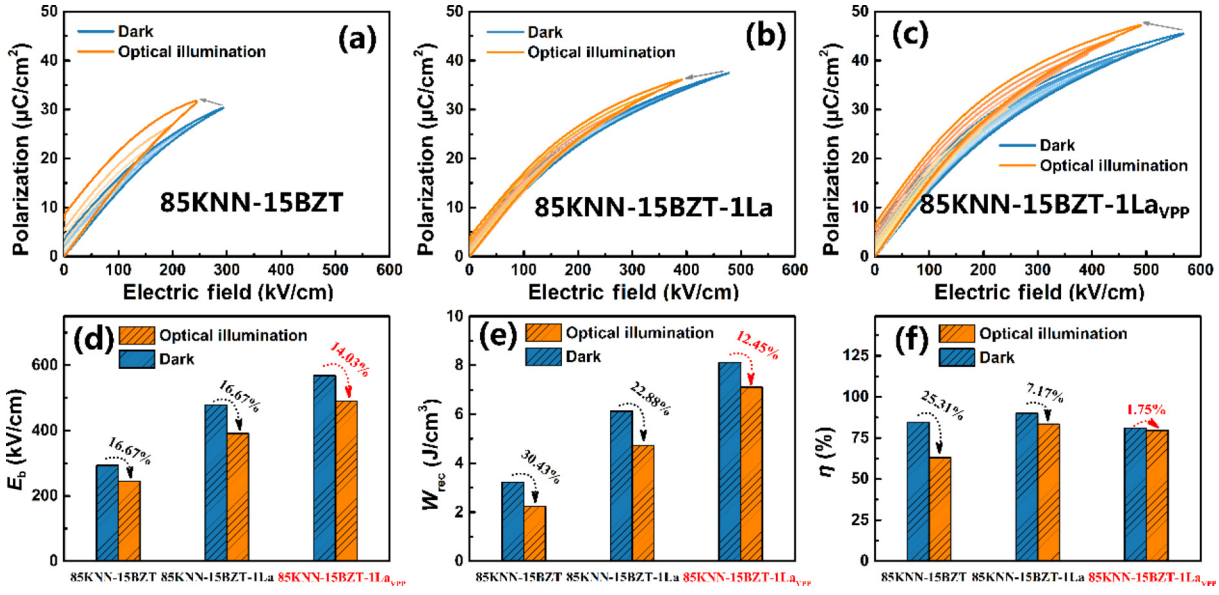

Fig. 6 Unipolar *P*–*E* loops under dark and optical illumination of (a) 85KNN–15BZT, (b) 85KNN–15BZT–1La, and (c) 85KNN–15BZT–1La$_{VPP}$ ceramics. comparison of (d) E_b, (e) W_{rec}, (f) η under different environmental conditions.

(Fig. 3(f)). Consequently, P_m of the 85KNN–15BZT–1La sample increased only slightly from 12.9 to 13.4 μC/cm² at the fixed electric field of 100 kV/cm, while the P_r value remains nearly unchanged (0.39 μC/cm² in dark and 0.45 μC/cm² under illumination). Furthermore, these excited electrons would significantly increase the leakage current in the ceramics, leading to a degradation of E_b, as shown in Fig. 6(d). The reduction in E_b for the 85KNN–15BZT–1La$_{VPP}$ sample is smaller than that observed in the other samples, likely due to the ceramics' high chemical homogeneity and compact microscopy. Consequently, the 85KNN–15BZT–1La$_{VPP}$ sample achieved stable W_{rec} and η values under illumination, with minor variations of 12.45% and 1.75%, respectively, achieved. The remarkable illumination resistance characteristics of the 85KNN–15BZT–1La$_{VPP}$ sample underscore its potential for applications in exposure environments.

4 Conclusions

In summary, the structure, dielectric, capacitive energy storage properties, and illumination resistance of 85KNN–15BZT–*x*La were systemically investigated. The optimized La dopant enhances the super paraelectric relaxor characteristic, reduces oxygen vacancies, and increases the band gap. As a result, excellent W_{rec} of 6.12 J/cm³ and high η of 89.87% are achieved under the electric field of 478 kV/cm in the 85KNN–15BZT–1La ceramics. Of particular importance is the further enhancement of energy storage properties to W_{rec} of 8.11 J/cm³, η of 80.98%, and E_b of 568 kV/cm through VPP. This improvement is attributed to higher chemical homogeneity, stronger relaxor behavior, and denser microstructure. In addition, the synergistic effects of low defect concentration, large band gap, high chemical homogeneity, and dense microcopy contribute to the excellent illumination resistance of W_{rec} and η, with a small variation of 12.45% and 1.75%. These results provide a promising avenue for the development of high-performance dielectric energy storage capacitors suitable for exposure environments.

Acknowledgements

The work was supported by the National Natural Science Foundation of China (Grant Nos. 52072150 and 51972146) and Shandong Province Key Fundamental Research Program (Grant No. ZR2022ZD39). The authors are grateful for the support from the Australian Synchrotron and thank Dr. Wenliang Tan and Qinfen Gu for their help during the experiments at the Australian Synchrotron.

Electronic Supplementary Material

Supplementary material is available in the online version of this article at https://doi.org/10.26599/JAC.2024.9220833.

Declaration of competing interest

The authors have no competing interests to declare that are relevant to the content of this article.

References

[1] Liu H, Liu YX, Song AZ, *et al.* (K,Na)NbO_3-based lead-free piezoceramics: One more step to boost applications. *Natl Sci Rev* 2022, **9**: nwac101.

[2] Lin JF, Cao YB, Zhu K, *et al.* Ultrahigh energy harvesting properties in temperature-insensitive eco-friendly high-performance KNN-based textured ceramics. *J Mater Chem A* 2022, **10**: 7978–7988.

[3] Wang G, Lu ZL, Li Y, *et al.* Electroceramics for high-energy density capacitors: Current status and future perspectives. *Chem Rev* 2021, **121**: 6124–6172.

[4] Zhao PY, Cai ZM, Wu LW, *et al.* Perspectives and challenges for lead-free energy-storage multilayer ceramic capacitors. *J Adv Ceram* 2021, **10**: 1153–1193.

[5] Yang LT, Kong X, Li F, *et al.* Perovskite lead-free dielectrics for energy storage applications. *Prog Mater Sci* 2019, **102**: 72–108.

[6] Xie AW, Fu J, Zuo RZ, *et al.* Supercritical relaxor nanograined ferroelectrics for ultrahigh-energy-storage capacitors. *Adv Mater* 2022, **34**: 2204356.

[7] Li DX, Zeng XJ, Li ZP, *et al.* Progress and perspectives in dielectric energy storage ceramics. *J Adv Ceram* 2021, **10**: 675–703.

[8] Pan H, Lan S, Xu SQ, *et al.* Ultrahigh energy storage in superparaelectric relaxor ferroelectrics. *Science* 2021, **374**: 100–104.

[9] Pan H, Li F, Liu Y, *et al.* Ultrahigh-energy density lead-free dielectric films via polymorphic nanodomain design. *Science* 2019, **365**: 578–582.

[10] Hu BB, Zhu MK, Guo JJ, *et al.* Origin of relaxor behavior in $K_{1/2}Bi_{1/2}TiO_3$–$Bi(Mg_{1/2}Ti_{1/2})O_3$ investigated by electrical impedance

spectroscopy. *J Am Ceram Soc* 2016, **99**: 1637–1644.
[11] Yuan QB, Li G, Yao FZ, *et al.* Simultaneously achieved temperature-insensitive high energy density and efficiency in domain engineered $BaTiO_3$–$Bi(Mg_{0.5}Zr_{0.5})O_3$ lead-free relaxor ferroelectrics. *Nano Energy* 2018, **52**: 203–210.
[12] Xing J, Huang YL, Xu Q, *et al.* Realizing high comprehensive energy storage and ultrahigh hardness in lead-free ceramics. *ACS Appl Mater Interf* 2021, **13**: 28472–28483.
[13] Zhang XT, Zhao LL, Liu LW, *et al.* Interface and defect modulation via a core–shell design in $(Na_{0.5}Bi_{0.5}TiO_3@La_2O_3)$–$(SrSn_{0.2}Ti_{0.8}O_3@La_2O_3)$–$Bi_2O_3$–$B_2O_3$–$SiO_2$ composite ceramics for wide-temperature energy storage capacitors. *Chem Eng J* 2022, **435**: 135061.
[14] Yang BB, Zhang Y, Pan H, *et al.* High-entropy enhanced capacitive energy storage. *Nat Mater* 2022, **21**: 1074–1080.
[15] Yan GW, Xu LQ, Fang BJ, *et al.* Achieving high pulse charge–discharge energy storage properties and temperature stability of $(Ba_{0.98-x}Li_{0.02}La_x)(Mg_{0.04}Ti_{0.96})O_3$ lead-free ceramics via bandgap and defect engineering. *Chem Eng J* 2022, **450**: 137814.
[16] Xie AW, Fu J, Zuo RZ, *et al.* $NaNbO_3$–$CaTiO_3$ lead-free relaxor antiferroelectric ceramics featuring giant energy density, high energy efficiency and power density. *Chem Eng J* 2022, **429**: 132534.
[17] Zhang M, Yang HB, Lin Y, *et al.* Significant increase in comprehensive energy storage performance of potassium sodium niobate-based ceramics via synergistic optimization strategy. *Energy Storage Mater* 2022, **45**: 861–868.
[18] Deng DJ, Irshad MS, Kong X, *et al.* Potassium sodium niobate-based transparent ceramics with high piezoelectricity and enhanced energy storage density. *J Alloys Compd* 2023, **953**: 170081.
[19] Peng X, Pu YP, Du XY, *et al.* Optical transmittance and energy storage properties of potassium sodium niobate glass-ceramics. *J Eur Ceram Soc* 2023, **43**: 966–973.
[20] Li W, Wang D, Li XF, *et al.* Optical temperature sensing properties and thermoluminescence behavior in Er-modified potassium sodium niobate-based multifunctional ferroelectric ceramics. *J Mater Chem C* 2022, **10**: 11891–11902.
[21] Qi H, Xie AW, Tian A, *et al.* Superior energy-storage capacitors with simultaneously giant energy density and efficiency using nanodomain engineered $BiFeO_3$–$BaTiO_3$–$NaNbO_3$ lead-free bulk ferroelectrics. *Adv Energy Mater* 2020, **10**: 1903338.
[22] Yang ZT, Gao F, Du HL, *et al.* Grain size engineered lead-free ceramics with both large energy storage density and ultrahigh mechanical properties. *Nano Energy* 2019, **58**: 768–777.
[23] Shao TQ, Du HL, Ma H, *et al.* Potassium–sodium niobate based lead-free ceramics: Novel electrical energy storage materials. *J Mater Chem A* 2017, **5**: 554–563.
[24] Huan Y, Wang XJ, Yang WY, *et al.* Optimizing energy harvesting performance by tailoring ferroelectric/relaxor behavior in KNN-based piezoceramics. *J Adv Ceram* 2022, **11**: 935–944.
[25] Xie AW, Qi H, Zuo RZ. Achieving remarkable amplification of energy-storage density in two-step sintered $NaNbO_3$–$SrTiO_3$ antiferroelectric capacitors through dual adjustment of local heterogeneity and grain scale. *ACS Appl Mater Interf* 2020, **12**: 19467–19475.
[26] Jiang J, Meng XJ, Li L, *et al.* Enhanced energy storage properties of lead-free $NaNbO_3$-based ceramics via A/B-site substitution. *Chem Eng J* 2021, **422**: 130130.
[27] Zhang N, Lv X, Zhang XX, *et al.* Feasible way to achieve multifunctional $(K,Na)NbO_3$-based ceramics: Controlling long-range ferroelectric ordering. *ACS Appl Mater Inter* 2021, **13**: 60227–60240.
[28] Xie AW, Zuo RZ, Qiao ZL, *et al.* $NaNbO_3$–$(Bi_{0.5}Li_{0.5})TiO_3$ lead-free relaxor ferroelectric capacitors with superior energy-storage performances via multiple synergistic design. *Adv Energy Mater* 2021, **11**: 2101378.
[29] Gao SQ, Wu SH, Zhang YG, *et al.* Study on the microstructure and dielectric properties of X9R ceramics based on $BaTiO_3$. *Mater Sci Eng B* 2011, **176**: 68–71.
[30] Li H, Meng QX, Gong DW, *et al.* Good temperature stability and high piezoelectric properties of pure and La-doped tetragonal $(K_{0.45}Na_{0.55})_{0.94}Li_{0.06}$-$Ta_xNb_{1-x}O_3$ ceramics. *J Eur Ceram Soc* 2014, **34**: 4185–4192.
[31] Bao J, Zhang XD, Fan B, *et al.* Ultrathin spinel-structured nanosheets rich in oxygen deficiencies for enhanced electrocatalytic water oxidation. *Angew Chem Int Edit* 2015, **54**: 7399–7404.
[32] Xiang K, Xu ZC, Qu TT, *et al.* Two dimensional oxygen-vacancy-rich Co_3O_4 nanosheets with excellent supercapacitor performances. *Chem Commun* 2017, **53**: 12410–12413.
[33] Luo XG, Yan ZN, Luo H, *et al.* Greatly improved piezoelectricity and thermal stability of (Na,Sm) Co-doped $CaBi_2Nb_2O_9$ ceramics. *Adv Powder Mater* 2023, **2**: 100116.
[34] Wang XZ, Huan Y, Zhao PY, *et al.* Optimizing the grain size and grain boundary morphology of $(K,Na)NbO_3$-based ceramics: Paving the way for ultrahigh energy storage capacitors. *J Materiomics* 2021, **7**: 780–789.
[35] Nobre MAL, Lanfredi S. Ferroelectric state analysis in grain boundary of $Na_{0.85}Li_{0.15}NbO_3$ ceramic. *J Appl Phys* 2003, **93**: 5557–5562.
[36] Gong HL, Wang XH, Zhang SP, *et al.* Grain size effect on electrical and reliability characteristics of modified fine-grained $BaTiO_3$ ceramics for MLCCs. *J Eur Ceram Soc* 2014, **34**: 1733–1739.
[37] Wang G, Li JL, Zhang X, *et al.* Ultrahigh energy storage density lead-free multilayers by controlled electrical homogeneity. *Energy Environ Sci* 2019, **12**: 582–588.
[38] Bidault O, Goux P, Kchikech M, *et al.* Space-charge relaxation in perovskites. *Phys Rev B* 1994, **49**: 7868–7873.
[39] Li M, Pietrowski MJ, De Souza RA, *et al.* A family of oxide ion conductors based on the ferroelectric perovskite $Na_{0.5}Bi_{0.5}TiO_3$. *Nat Mater* 2014, **13**: 31–35.
[40] Chan NH, Sharma RK, Smyth DM. Nonstoichiometry in undoped $BaTiO_3$. *J Am Ceram Soc* 1981, **64**: 556–562.
[41] Waser R. Bulk conductivity and defect chemistry of acceptor-doped strontium titanate in the quenched state. *J Am Ceram Soc* 1991, **74**: 1934–1940.
[42] Molak A, Ksepko E, Gruszka I, *et al.* Electric permittivity and conductivity of $(Na_{0.5}Pb_{0.5})(Mn_{0.5}Nb_{0.5})O_3$ ceramics. *Solid State Ion* 2005, **176**: 1439–1447.
[43] Tauc J, Grigorovici R, Vancu A. Optical properties and electronic structure of amorphous germanium. *Phys Status Solidi B* 1966, **15**: 627–637.
[44] Wang M, Feng Q, Luo CY, *et al.* Ultrahigh energy storage density and efficiency in $Bi_{0.5}Na_{0.5}TiO_3$-based ceramics via the domain and bandgap engineering. *ACS Appl Mater Interfaces* 2021, **13**: 51218–51229.
[45] Dai ZH, Li DY, Zhou ZJ, *et al.* A strategy for high performance of energy storage and transparency in KNN-based ferroelectric ceramics. *Chem Eng J* 2022, **427**: 131959.
[46] Liu J, Wang Y, Zhu H, *et al.* Synergically improved energy storage performance and stability in sol–gel processed $BaTiO_3$/$(Pb,La,Ca)TiO_3$/$BaTiO_3$ tri-layer films with a crystalline engineered sandwich structure. *J Adv Ceram* 2023, **12**: 2300–2314.
[47] Hu QY, Tian Y, Zhu QS, *et al.* Achieve ultrahigh energy storage performance in $BaTiO_3$–$Bi(Mg_{1/2}Ti_{1/2})O_3$ relaxor ferroelectric ceramics via nano-scale polarization mismatch and reconstruction. *Nano Energy* 2020, **67**: 104264.
[48] Yan XD, Zheng MP, He Y, *et al.* Origin of superior dielectric and piezoelectric properties in $0.4Ba(Zr_{0.2}Ti_{0.8})O_3$–$0.6(Ba_{0.7}Ca_{0.3})TiO_3$ at intermediate grain sizes. *J Eur Ceram Soc* 2020, **40**: 3936–3945.
[49] Huan Y, Wang XH, Fang J, *et al.* Grain size effects on piezoelectric properties and domain structure of $BaTiO_3$ ceramics prepared by two-step sintering. *J Am Ceram Soc* 2013, **96**: 3369–3371.
[50] Calisir I, Amirov AA, Kleppe AK, *et al.* Optimisation of functional properties in lead-free $BiFeO_3$–$BaTiO_3$ ceramics through La^{3+} substitution strategy. *J Mater Chem A* 2018, **6**: 5378–5397.
[51] Lente MH, Eiras JA. Interrelationship between self-heating and ferroelectric properties in PZT ceramics during polarization reorientation. *J Phys Condens Matter* 2000, **12**: 5939–5950.
[52] Ishibashi Y. A model of polarization reversal in ferroelectrics. *J Phys Soc Jpn* 1990, **59**: 4148–4154.
[53] Lente MH, Picinin A, Rino JP, *et al.* 90° domain wall relaxation and frequency dependence of the coercive field in the ferroelectric switching process. *J Appl Phys* 2004, **95**: 2646–2653.